Chinese Chemical Letters 37 (2026) 111438

Contents lists available at ScienceDirect

Chinese Chemical Letters

journal homepage: www.elsevier.com/locate/cclet

# Double-shelled $CeO_x$/CoS hollow nanobox for synergistic inhibition of polysulfides shuttle effect and lithium dendrites in robust lithium-sulfur battery

Xinyun Liu[a,b,c], Long Yuan[b], Xiaoli Peng[b], Shengjun Lu[b], Shilan Li[b], Shengdong Jing[b], Hua Lei[b,*], Yufei Zhang[a,*], Haosen Fan[c,*]

[a] School of Chemical Engineering and Light Industry, Guangdong University of Technology, Guangzhou 510006, China
[b] College of Materials Science and Metallurgy Engineering, Guizhou University, Guiyang 550025, China
[c] School of Chemistry and Chemical Engineering, Guangzhou University, Guangzhou 510006, China

ARTICLE INFO

*Article history:*
Received 14 May 2025
Revised 9 June 2025
Accepted 10 June 2025
Available online 10 June 2025

*Keywords:*
Li-S batteries
$CeO_x$/CoS
Separator modification
Catalytic conversion and chemisorption
$CeO_x$ nanodots

ABSTRACT

Li-S batteries (LSBs) offer significant promise for next-generation energy storage systems on account of their high energy density and the high capacity of sulfur. Nevertheless, the severe shuttle effect of lithium polysulfide (LiPSs) and the sluggish reaction kinetics greatly hinder the further application of LSBs. In this manuscript, Hollow $CeO_x$/CoS core-shell hybrid were designed and synthesized using ZIF-67 as the self-template to prepare hollow CoS dodecahedral nanoboxs and the subsequent generation of $CeO_x$ nanodots. When used as the polyolefin separator modifier, the unique dodecahedral structure of hollow CoS/$CeO_x$ presents large specific surface area, abundant porous structure and enough active sites, which not only ensures the fast transport of electrolyte/ions and offers numerous active catalytic sites to accelerate the reaction kinetics of LiPSs. In addition, the catalytic activity of the $CeO_x$/CoS hybrid greatly enhance the uniform ion diffusion and stable growth of lithium nucleation on the lithium metal anode side. The cell with $CeO_x$/CoS modified separator presented excellent long cycle stability and satisfactory rate performance. The battery can maintain the capacity of 502.2 mAh/g after 900 cycles at the current density of 1 C, accompanying by a minimal 2 decay rate of 0.057 %. Even at a current density of 3 C, a high specific capacity of 735.58 mAh/g can still obtained. Besides, when the sulfur loading increase into 4.480 mg/cm$^2$, the battery still can maintain excellent cycling stability with the capacity retention ratio of 94.5 % after 100 cycles. This study will provide new strategy for the design and preparation of heterostructure with outstanding catalytic performance for LSBs.

© 2026 Published by Elsevier B.V. on behalf of Chinese Chemical Society and Institute of Materia Medica, Chinese Academy of Medical Sciences.

Due to the rapid development of electric vehicles, portable electronic devices and grid energy technology, traditional lithium-ion batteries (LIBs) have hardly satisfied the ever-increasing demand because of their low theoretical capacity and the shortage/maldistribution of lithium resources [1]. Hence, it is necessary to develop the new generation of rechargeable batteries with high energy density to meet the increasing needs of energy storage systems [2–6]. Lithium-sulfur batteries (LSBs) are regarded as one of the highly promising candidates because of their high theoretical specific capacity (1675 mAh/g) and high specific energy density (2600 Wh/kg), along with the plentiful natural reserves of sulfur cathode, low cost and environmental friendliness [7–10]. However, LSBs are also faced with some key problems including low sulfur utilization, poor coulomb efficiency and short cycle life [11], which are mainly caused by the following aspects: (1) Poor conductivity of sulfur, large volume expansion (79 %) during the cycling process and the sluggish reaction kinetics [12–14]; (2) The "shuttle effect" caused by the intermediate reaction product soluble lithium polysulfide (LiPSs, $Li_2S_n$, $4 \leq n \leq 8$) produced in the process of redox leads to rapid capacity attenuation [15,16]; (3) Polysulfide lithium is easily dissolved in the electrolyte and migrates to the lithium anode, forming insoluble $Li_2S$/$Li_2S_2$, resulting in low sulfur utilization and the formation of lithium dendrites [17–20]. To date, a variety of strategies have been developed to address these obstacles, with much work devoted to the design of high-performance sulfur cathode hosts [21–23], electrolyte optimization [24], lithium anode protection [25], and separator modification [26–28]. The sulfur cathode body is designed to physically

* Corresponding authors.
*E-mail addresses:* Leihua_gzu@163.com (H. Lei), yfzhang@gdut.edu.cn (Y. Zhang), hsfan@gzhu.edu.cn (H. Fan).

https://doi.org/10.1016/j.cclet.2025.111438
1001-8417/© 2026 Published by Elsevier B.V. on behalf of Chinese Chemical Society and Institute of Materia Medica, Chinese Academy of Medical Sciences.

confine polysulfide lithium to the sulfur cathode body by introducing porous carbon-based materials [29], metal oxides [30], nitrides [31] and sulfides [32] into the cathode. However, the introduction of a large number of main materials has a great impact on the energy density of the battery, and the electrochemical performance is poor [33]. As a key component between the cathode and anode in LSBs, the separator can avoid short circuit of the battery, provide an effective ion transport channel, and exclude electron transport [34,35]. The commonly used commercial polypropylene (PP) separator has a poor ability to limit dissolved LiPSs due to their large nanopore, and the pp separator has a poor affinity for LiPSs, resulting in still shuttling to the lithium anode [36]. Therefore, the addition of functional coatings between the separator is considered to be a simple and effective strategy, including non-polar carbon materials, such as porous carbon, graphene oxides (GOs), carbon nanotubes (CNTs) and non-carbonized materials, such as metal oxides, sulfides, and nitrides [37–40]. These functional coatings can not only effectively inhibit the dissolution of LiPSs and the uneven deposition of lithium ions, but also inhibit the shuttle effect of LiPSs through the strong interaction with polysulfide to promote its chemisorption and catalytic conversion, so as to obtain high-performance LSBs [41].

In recent years, metal-organic frameworks (MOFs) have attracted extensive attention due to their unique structures and diverse functionalities, making them the promising candidates in many fields such as catalysis, sensors, energy storage and electrocatalysis [42–46]. Notably, some reports have demonstrated that the construction of modified layer from MOFs and their derived materials can effectively improve the electrochemical and battery performances in LSBs. Recently, rare earth oxides such as cerium oxides ($CeO_x$) have been widely used in electrocatalysis because of their superior electron-ion conductivity and favorable oxygen storage capacity [47]. The reversible oxygen ion exchange on the surface of cerium oxide, which can switch between $Ce^{4+}$ and $Ce^{3+}$ oxidation states, which contribute the excellent catalytic activity. In addition, the proper concentration of oxygen vacancies gives the $CeO_x$ catalysts a higher redox capacity [48]. They can significantly enhance the chemical anchoring ability of LiPSs and accelerate the redox kinetics of LiPSs by reducing the $Li_2S$ decomposition energy barrier. However, $CeO_x$ nanoparticles are prone to agglomeration and have a low specific surface area, making it difficult to construct a continuous conductive network. The combination of MOF-derived carbon and $CeO_x$ can form a synergistic interface: The carbon skeleton provides a three-dimensional conductive path and a physical constraint framework, while the oxygen vacancies on the surface of $CeO_x$ act as active sites to promote the adsorption-catalytic cycle of LiPSs. However, they are less reports on the incorporation of $CeO_x$ with MOF derivatives to realize the co-catalytic effect in LSBs.

In this study, we designed and synthesized double-shelled $CeO_x$/CoS hollow nanobox through the growth of $CeO_x$ nanodots (NDs) on the surface of ZIF-67 derived CoS nanobox. When served as the modified layer for polyolefin separator, the multifunctional separator ($CeO_x$/CoS@PP) can provide large surface area, more active sites, high electrolyte wettability, which ensure fast pathways for electrolyte/ions and improved electrocatalytic activity. Besides, $CeO_x$ nanodots could anchor the soluble LiPSs through physical blocking or chemisorption on the cathode side to inhibit the shuttling effect, as well as promoting the catalytic conversion of LiPSs to $Li_2S_2$/$Li_2S$ and accelerating the sulfur redox kinetics. In addition, the catalytic activity of hollow $CeO_x$/CoS hybrid nanoboxs is greatly improved, and uniform ion diffusion and stable lithium nucleation growth on the anode side of lithium metal can also be achieved. As a result, the modified battery equipped with the $CeO_x$/CoS@PP separator provides an initial specific capacity of 1093.9 mAh/g at a current of 0.5 C, with a decay rate of 0.10 % after 400 cycles. Cycle performance is greatly improved at 1 C with a capacity of 502.2 mAh/g after 900 cycles, showing an ultra-low attenuation rate of 0.057 %. When the sulfur loading reached as high as 4.480 mg/cm$^2$, the battery can still remain distinguished cyclic stability after 100 cycles with the capacity retention rate of 94.5 %.

The detailed preparation process of $CeO_x$/CoS is shown in Scheme S1 (Supporting information). Firstly, we synthesized Co-based zeolite imidazolate framework (ZIF67) with a uniform rhombic dodecahedral nanocrystal structure as a precursor by a self-assembly method. After that, the ZIF-67 nanoparticles underwent homogeneous redispersion in an ethanol solution containing thioacetamide (TAA) using sonication and refluxed at elevated temperatures, resulting in the formation of an amorphous CoS hollow nanobox around the framework of each ZIF67 particle. Secondly, a mixed solution containing hollow CoS, cerium nitrate, and hexamethylenetetramine (HMT) was heated at 180 °C for 6 h by hydrothermal method to induce an *in-situ* surface coating process, during which the *in-situ*-generated $CeO_x$ nanodots ($CeO_x$ NDs) were firmly anchored on the surface of the CoS hollow nanoboxs. $Ce^{3+}$ hydrolyzes in the HMT system to generate $CeO_x$ nanodots that anchor on the surface of the CoS hollow nanobox ($CeO_x$/CoS). The abundant oxygen vacancies on its surface form a strong electronic coupling with the sulfur defect sites of CoS, constructing the Ce-O-S-Co heterointerface.

Scanning electron microscopy (SEM) and transmission electron microscopy (TEM) were used to characterize the surface morphology and microstructure of all samples at different magnifications (Figs. 1a-c and Fig. S1 in Supporting information). As shown in Figs. 1a and b, ZIF-67 exhibits a well-defined rhombohedral nanocrystal structure with an average particle size of about 500 nm, and a hollow nanobox with a thickness of about 20 nm was formed around the ZIF-67 nanoparticles after vulcanization. The *in situ* grown $CeO_x$ NDs were uniformly dispersed on the hollow CoS nanoboxs can be seen in Fig. 1c. The growth of $CeO_x$ nanodots on the CoS surface is due to the fact that the large surface area of CoS contains abundant amino groups that can serve as nucleation sites, while the HMT surface also has a large number of amino groups as dispersants, which leads to the uniform deposition of $CeO_x$ on CoS under thermal reduction conditions. the hollow $CeO_x$/CoS core-shell structures were further demonstrated by TEM images (Figs. 1d and e, Fig. S2 in Supporting information), the $CeO_x$ NDs are uniformly dispersed on the hollow CoS dodecahedron with a highly porous structure. The nitrogen adsorption-

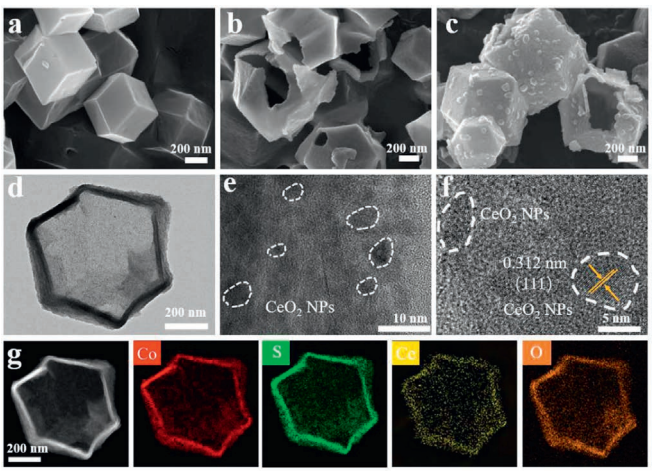



**Fig. 1.** (a) SEM images of ZIF-67 precursor. (b) SEM images of CoS nanoboxs. (c) SEM images of $CeO_x$/CoS NDs. (d-f) TEM images at different magnifications of $CeO_x$/CoS NDs. (g) High-angle annular dark field (HAADF) of $CeO_x$/CoS and corresponding elemental mapping images of Co, S, Ce and O.

desorption isotherm indicated that the surface area measures 91.70 $m^2/g$, with the pore size distribution predominantly concentrated in the mesoporous regions of 2.16 and 12.46 nm (Fig. S3 in Supporting information). Mesoporous structures enhance the performance of LSBs through three aspects: physical confinement, chemical adsorption, and ion transport optimization. 2.16 nm mesopores are strongly anchored for LiPSs, suitable for high sulfur loads and long cycles. 12.46 nm mesopores provide efficient ion transport, suitable for high rates and volume expansion buffering. Under high-resolution transmission electron microscopy (HRTEM, Fig. 1e), lattice streaks of $CeO_x$ planes with spacings of 0.312 nm corresponding to the (111) plane of $CeO_x$ NDs, respectively, and a tiny crystal lattice of the surrounding CoS are shown, which suggests that the $CeO_x$ NDs are on the CoS substrate well-grown (Fig. 1f). As shown in Fig. S4 (Supporting information), the selected area electron diffraction (SAED) pattern shows multiple rings, consistent with the polycrystalline structure of $CeO_x$ NDs in HRTEM. More importantly, polycrystalline $CeO_x$/CoS can be observed under high-angle annular dark-field scanning transmission electron microscopy (HAADF-STEM) (Fig. 1g), and furthermore, the elemental distributions of $CeO_x$/CoS were determined using energy-dispersive X-ray spectroscopy (EDS) mapping, and the images show the coexistence and uniform distribution of each element of Co, S, Ce, and O in this heterostructure. In the nanohybrid structure with $CeO_x$ NDs decorating hollow CoS, the large surface area of CoS, the abundant porous structure and its huge cavity not only provide fast channels for electrolyte and ions, but also more electrocatalytically active sites to promote the catalytic conversion of LiPSs, whereas the $CeO_x$ NDs as a functional layer not only anchor the soluble LiPSs on the cathode side to physically blocking or chemisorption to inhibit their shuttling, but also promote the catalytic conversion of LiPSs to $Li_2S_2/Li_2S$ and accelerate the sulfur redox kinetics. An electronic reconstruction effect is formed between $CeO_x$ and CoS through strong interfacial coupling: The $Ce^{3+}/Ce^{4+}$ redox pair can adjust the electron density of the Co-S bond, while the synergistic effect of surface S-O defects and oxygen vacancies significantly enhances the chemical anchor-binding ability of LiPSs, providing efficient active sites for the adsorption-catalytic conversion of LiPSs and accelerating the kinetics of redox reactions.

The detailed crystal structures as well as the chemical compositions of all materials were then analyzed in depth by XRD and XPS. As shown in the XRD patterns of Fig. S5a (Supporting information), each peak of ZIF67 corresponds to its standard PDF card, which proved that the successful preparation of the ZIF67 precursor, whereas the pattern of CoS proved its amorphous nature, and we were not able to detect the signals of CoS nanoboxs. In addition, it turns out that the signals of the CoS shells in the $CeO_x$/CoS samples are also not accompanied by the peaks of $CeO_x$, the peaks of 28.5°, 33.1°, and 47.4° observed from the pattern should be attributed to the (111), (200), and (220) facets in the $CeO_2$ crystals. (PDF #34–0394), which indicated the existence of an ultrafine crystal structure of $CeO_x$ [49]. All of evidences confirms that we successfully fabricated the target products. The detailed chemical composition and electronic states of $CeO_x$/CoS were further illustrated using the XPS method (Figs. S5b-f in Supporting information). Fig. S5b shows the survey spectrum of $CeO_x$/CoS including elements of Ce, Co, O, N, C and S, which is in agreement with the results of the above XRD pattern, and further proved the successful preparation of $CeO_x$/CoS. We corrected with the C 1s peak at 284.8 eV, and the peaks of C 1s at 288.5, 286, and 284.8 eV belong to C–C, C–C-O, and C–C=O, respectively (Fig. S5f). As can be observed in Fig. S5c, the high-resolution XPS spectrum of Ce 3d in $CeO_x$/CoS shows the spin-orbit splitting of Ce $3d_{5/2}$ and Ce $3d_{3/2}$, which typically consists of $Ce^{3+}$ and $Ce^{4+}$. Specifically, the peak at a binding energy of about 903.8 eV in Ce $3d_{3/2}$ is assigned to $Ce^{3+}$, and another peak assigned to $Ce^{4+}$ is located at 917.2 eV, and in this way, the peaks at 900.8 and 882.2 eV in Ce $3d_{5/2}$ are assigned to $Ce^{4+}$, while the peak assigned to $Ce^{3+}$ is located at 886.2 eV. As shown in Fig. S5d, both $Co^{2+}$ and $Co^{3+}$ were present in the high-resolution spectra of Co 2p, where two sets of peaks were assigned to Co $2p_{3/2}$ and Co $2p_{1/2}$. Notably, the binding energy peaks of $Co^{2+}$ and $Co^{3+}$ were about 795.8 and 794.3 eV in Co $2p_{1/2}$, and about 781.2 and 779.7 eV in Co $2p_{3/2}$. In addition, the XPS spectrum of S 2p as shown in Fig. S5e, demonstrates peaks mainly located at 161.5 and 163.2 eV, which correspond to the binding energies of S $2p_{3/2}$ and S $2p_{3/2}$ in the Co-S band, respectively, whereas the binding energy of 168.9 eV could be assigned to the S-O band, which came from adsorption of CoS surface of the solvent or oxidized S in the air atmosphere. All of the above evidences indicated the successful construction of this target hybridization system by the deposition of $CeO_x$ NDs on hollow CoS. By introducing Ce into CoS, the deposited $CeO_x$ layer can effectively protect CoS and make it more stable. This coordination defect condition of S-O, for example, is expected to generate more sulfur vacancies and oxygen vacancies, resulting in enhanced electrocatalytic activity.

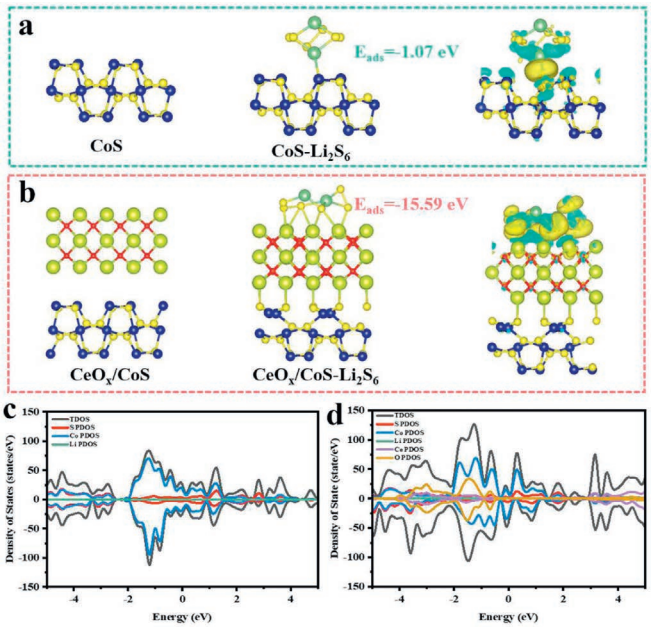



**Fig. 2.** The DFT calculation of the adsorption energy for $Li_2S_6$ and their differential charge densities of (a) CoS and (b) $CeO_x$/CoS. The density of states distribution curves of (c) CoS and (d) $CeO_x$/CoS for $Li_2S_6$.

In order to show a deep understanding of how the oxygen vacancies and sulfur vacancies in $CeO_x$/CoS cooperatively promote the adsorption and transformation of LiPSs, the models such as $CeO_x$/CoS and CoS were calculated and analyzed based on density functional theory (DFT) (Fig. 2). From the perspective of adsorption energy, the adsorption energy of the $CeO_x$/CoS system for $Li_2S_6$ is −15.59 eV (Fig. 2b), which is 93 % higher than that of CoS (−1.07 eV) (Fig. 2a). This indicates that the synergistic effect of oxygen vacancies and sulfur vacancies significantly enhances the adsorption capacity for LiPSs, and electrostatic attraction and ionic bonding make the adsorption more stable. Differential charge density shows that oxygen vacancies cause the loss of electrons near Ce to form Lewis acid sites, while sulfur vacancies increase the electron density around Co to form Lewis base sites. The two form a “double anchoring” effect through charge transfer, enhancing the adsorption strength of the LiPSs. In addition, the heterojunction defect network formed by oxygen vacancies and sulfur vacancies increases the density of active catalytic sites for LiPSs. In terms of density of states (Figs. 2c and d), oxygen vacancies in-

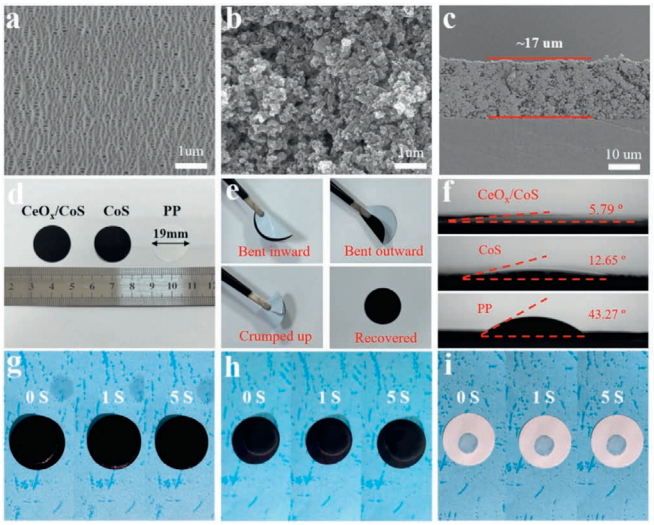



**Fig. 3.** (a) SEM images of the surface of commercial pp separator and (b) $CeO_x$/CoS modified separator. (c) Cross-sectional SEM image of $CeO_x$/CoS modified separator. (d) Digital photograph of the appearance of the different separators. (e) Flexural mechanical properties of $CeO_x$/CoS modified separator. (f) Contact angle of three separators on electrolyte. Wetting performance of (g) $CeO_x$/CoS@PP, (h) CoS@PP and (i) PP separators on electrolyte.

crease the density of states of the d orbitals of Ce near the Fermi level, while sulfur vacancies shift the density of states of the d orbitals of Co towards the lower energy region. The hybridization of the two orbitals is enhanced, forming an electron transport channel, reducing the activation energy for LiPSs conversion, and accelerating the reaction. In conclusion, the oxygen and sulfur vacancies in $CeO_x$/CoS significantly enhance the adsorption capacity for LiPSs through electrostatic synergy, electronic structure optimization, and complementary active sites, and accelerate their conversion process.

We explored the physical properties of different separators by the following experiments. From the comparison of the surface SEM images (Figs. 3a and b), it can be visualized that the surface of the commercial PP separator display the uniformly distributed reticulation structure with large number of pores that are larger than the diameter of LiPSs, which would result in the inability to block its access to the lithium anode and inhibit the electron transfer, and after coating a layer of $CeO_x$/CoS material on the PP separator, the pores on its surface are uniformly covered by nanoparticles, which is more effective in terms of physical blocking for suppressing the shuttle effect of LiPSs. From the cross-sectional SEM image of the modified diaphragm (Fig. 3c), it can be observed that the thickness of the coating layer averages 17 μm. We took digital photos of the different separators. Fig. 3d shows that all three separators have a diameter of 19 mm, and the $CeO_x$/CoS@PP separator is a uniformly textured nano-coating over PP. In order to verify the mechanical properties of the $CeO_x$/CoS@PP separator even further, we performed multiple folding tests. It can be observed that the $CeO_x$/CoS modified layer did not come off from the PP separator after multiple folding from Fig. 3e, and the modified separator remained intact. The results proved that the adhesion between $CeO_x$/CoS modified material and PP separator was satisfactory, and the $CeO_x$/CoS@PP separator had excellent toughness. Furthermore, we tested the wettability of three separators to the electrolyte by adding drops of electrolyte to their surfaces and observing their contact angles. It can be directly observed that the PP separator has the worst wettability with a contact angle of 43.27°, both $CeO_x$/CoS@PP and CoS@PP separators have significantly improved affinity for the electrolyte with contact angles of 5.79° and 12.65° (Fig. 3f), respectively. It can be seen from the electrolyte immersion experiment in Figs. 3g-i, the electrolyte diffused the fastest on the $CeO_x$/CoS@PP separator with the largest infiltration area (Fig. 3g). The above results indicate that the $CeO_x$/CoS@PP separator increased the affinity with the electrolyte. The significant improvement in wettability is attributed to: (1) The abundant hydroxyl groups on the surface of $CeO_x$ form strong hydrogen bonds with ether electrolytes; (2) The ion sieving effect of the multi-level pores in the coating reduces the interfacial transport resistance.

LSBs with different modified separators were assembled and their electrochemical performances were investigated, and the results showed that the $CeO_x$/CoS@PP batteries exhibited commendable performances, including long-cycle stability, excellent rate performance, cycling stability under high sulfur loading, and good resistance to self-discharge. As shown in Fig. 4a, the $CeO_x$/CoS@PP battery has an initial specific capacity of 1093.91 mAh/g at 0.5 C and still maintains a specific capacity of 640.31 mAh/g after 400 cycles with a decay rate of 0.10% per cycle, which is much higher than the CoS@PP battery with a decay rate of 0.12% per cycle (specific capacity after cycling of 413.95 mAh/g) and the PP battery with a decay rate of 0.14% per cycle (specific capacity after cycling of 298.04 mAh/g). In additionally, the Coulombic efficiency of the $CeO_x$/CoS@PP battery has been maintained at a stable level higher than 99%, and the promising cycling stability indicates that $CeO_x$/CoS@PP has a strong chemisorption effect on LiPSs and promotes its catalytic conversion. The correctness of this analysis is supported by further investigation of its long-cycle performance and rate performance. With the current density increased to 1 C (Fig. 4c), the $CeO_x$/CoS@PP battery still exhibits an initial specific capacity of 1050.31 mAh/g and superb cycling stability, it still maintains a specific capacity of 500.21 mAh/g after 900 cycles, demonstrating an ultra-low degradation rate of 0.058% per cycle. The result is far superior to the CoS@PP battery (194.29 mAh/g capacity after cycling) with a decay rate of 0.086% per cycle and the 0.087% decay rate per cycle for PP battery (131.817 mAh/g capacity after cycling). It is further emphasized that $CeO_x$/CoS plays an important role in the long cycle stability through its unique structure and strong electrocatalytic activity. The rate performance of different separators is shown in Figs. 4b, d, f and Fig. S6 (Supporting information), which can be used to analyze the kinetics of redox reactions on the separator surface. Satisfactorily, the battery using $CeO_x$/CoS@PP separator achieved discharge specific capacities of 1362.3, 1142.2, 1036.7, 886.5, and 735.6 mAh/g at current densities of 0.2, 0.5, 1, 2, and 3 C, respectively, which were far superior to those of the CoS@PP and PP batteries (Fig. 4b). It is commendable that $CeO_x$/CoS@PP battery can also maintain a high specific capacity of 1197.2 mAh/g when the current density is restored to 0.2 C, indicating that the introduction of $CeO_x$/CoS@PP improves the rate performance of the cells at different current densities. Furthermore, the above analysis can also be verified by the galvanostatic charge/discharge (GCD) curves at different current densities, and the $CeO_x$/CoS@PP battery has the highest specific capacity as well as the smallest polarization voltage (Fig. 4d), which suggests that it is more susceptible to the conversion of LiPSs to $Li_2S_2$ or $Li_2S$ to accelerate the kinetics of the redox reaction. This phenomenon can be attributed to the synergistic catalytic effect of $CeO_x$/CoS heterostructures on LiPSs: On the one hand, the hierarchical porous structure effectively inhibits the shuttle effect of LiPSs through physical confinement; On the other hand, the synergistic effect of the redox pairs of $Ce^{3+}/Ce^{4+}$ and $Co^{2+}/Co^{3+}$ significantly reduces the activation energy barrier of the $Li_2S$ nucleation/decomposition process, thereby accelerating the conversion kinetics of LiPSs to $Li_2S_2$ or $Li_2S$. The cycling performances of $CeO_x$/CoS@PP battery at 0.5 C with high sulfur loading were shown in Fig. 4e. Its capacity remained at 772.7 mAh/g and the capacity retention was 94.5% at a sulfur loading of 2.304 mg/cm$^2$ after 100 cycles. When the sulfur loading was increased to 3.328 mg/cm$^2$,

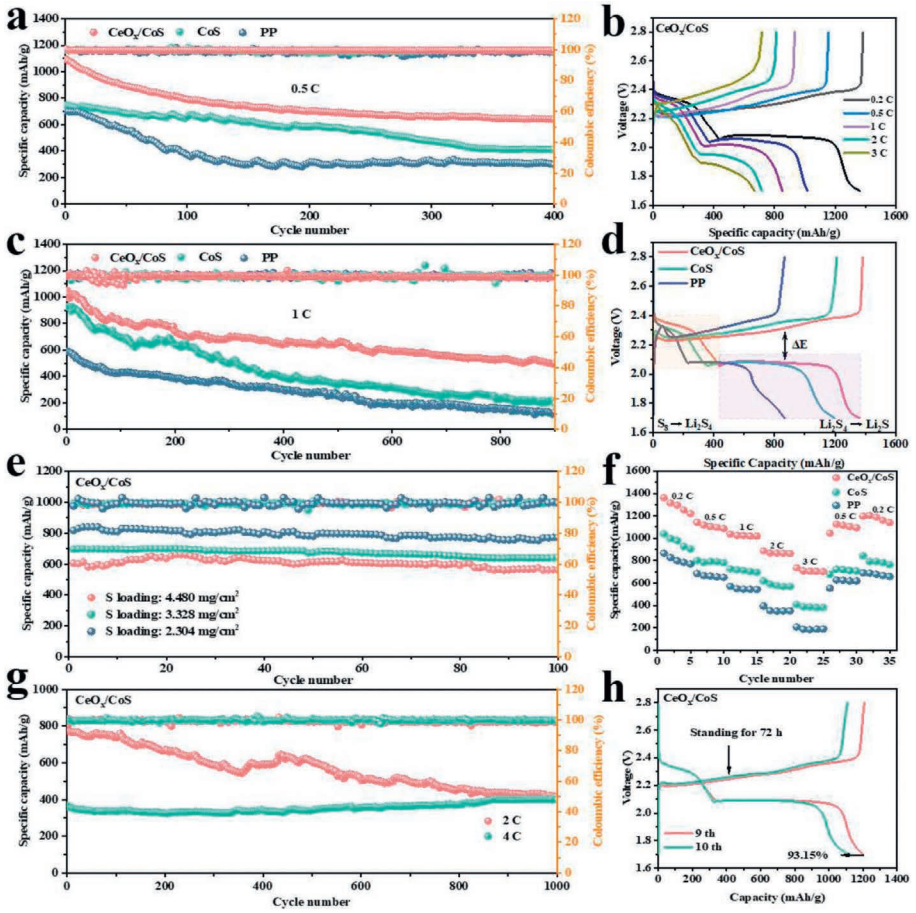



**Fig. 4.** (a) Cycling performance at 0.5 C and (b, d, f) rate performance of Li-S batteries assembled by different separators. (c) Long cycle performance of different separators at 1 C current density. (e) Cycle performance of $CeO_x$/CoS@PP separator at 0.5 C with different high sulfur loading. (g) Cycling stability of $CeO_x$/CoS@PP separator at high current density. (h) Typical discharge-charge voltage curves revealing self-discharge behavior after standing for 72 h.

the capacity retention was 92.3 %, and even after the sulfur loading was increased to 4.480 mg/cm$^2$, it maintained a strong cycling stability with 92.8 % capacity retention. Additionally, the $CeO_x$/CoS@PP also showed excellent performance in the long-cycle test of 1000 cycles at 2 C and 4 C with the discharge specific capacity remaining at 414.3 and 398.8 mAh/g (Fig. 4g), and the Coulombic efficiencies exceeding 99.8 % in both cases, which further demonstrated that even at high current densities, the $CeO_x$/CoS@PP separator can also achieve high-quality catalytic conversion. All the above results are attributed to the special structure and strong catalytic performance of $CeO_x$/CoS to promote the catalytic conversion of LiPSs and accelerate the redox reaction process, which enables the battery to maintain a high specific capacity and slow capacity decay after long cycles, showing a strong long cycle life. It is worth noting that the self-discharge phenomenon in the battery is also a difficult problem that affects the cycle performance. We observed the self-discharge phenomena of batteries with different separators after standing them for 72 h, the specific discharge capacity of the $CeO_x$/CoS@PP battery was 1118.7 mAh/g and the capacity retention rate was 93.15 % (Fig. 4h). This result was higher than that of CoS@PP battery with capacity retention rate of 89.73 % and PP battery with capacity retention rate of 88.14 % (Fig. S7 in Supporting information), indicating that the introduction of $CeO_x$/CoS@PP can effectively control self-discharge phenomenon. Furthermore, we conducted multi-dimensional comparisons of the electrochemical performance of this work and other works, proving that this work has excellent long-cycle stability, coulombic efficiency and rate performance (Fig. S8 in Supporting information).

In order to further investigate the electrocatalytic effect of $CeO_x$/CoS@PP on LSBs, cyclic voltammetry (CV) and electrochemical impedance spectroscopy (EIS) were employed to test different separator batteries. As shown in Fig. 5a, the presence of two cathodic peaks and one anodic peak can be clearly observed in the CV curves at a scan rate of 0.1 mV/s. The cathodic peaks (reduction peaks) at voltages around 2.0 and 2.3 V indicate that the reduction of $Li_2S_8$ first to $Li_2S_6$ or $Li_2S_4$ and then further to $Li_2S_2$ or $Li_2S$. Meanwhile, the anodic peak (oxidation peak) near the voltage of 2.4 V indicates that the process of $Li_2S_2$ or $Li_2S$ being oxidized to soluble LiPSs and then further oxidized to solid $S_8$. It can be clearly observed that the $CeO_x$/CoS@PP battery has the highest peak current and the smallest polarization potential at the cathodic and anodic peaks compared to the CoS@PP and PP batteries, which confirms that the $CeO_x$/CoS@PP separator has an improving and accelerating effect on the kinetics of the redox reaction, and it plays an extremely important role in promoting the catalytic conversion of polysulfides. The CV curves for the first three cycles of $CeO_x$/CoS@PP at a scan rate of 0.1 mV/s were highly overlapping, indicating good stability as well as reversibility (Fig. 5b). In order to further investigate the $Li^+$ diffusion ability, the CV curves of different separator batteries were tested at different scan rates from 0.1 mV/s to 0.5 mV/s. Compared with CoS@PP (Fig. 5d) and PP batteries (Fig. S9 in Supporting information), the CV curves of $CeO_x$/CoS@PP batteries exhibited higher peak currents and the smaller polarization voltages at all the scan rates (Fig. 5c). We performed a linear fit of the square root of the scan rate to the peak current based on the CV curves of the three separators at different

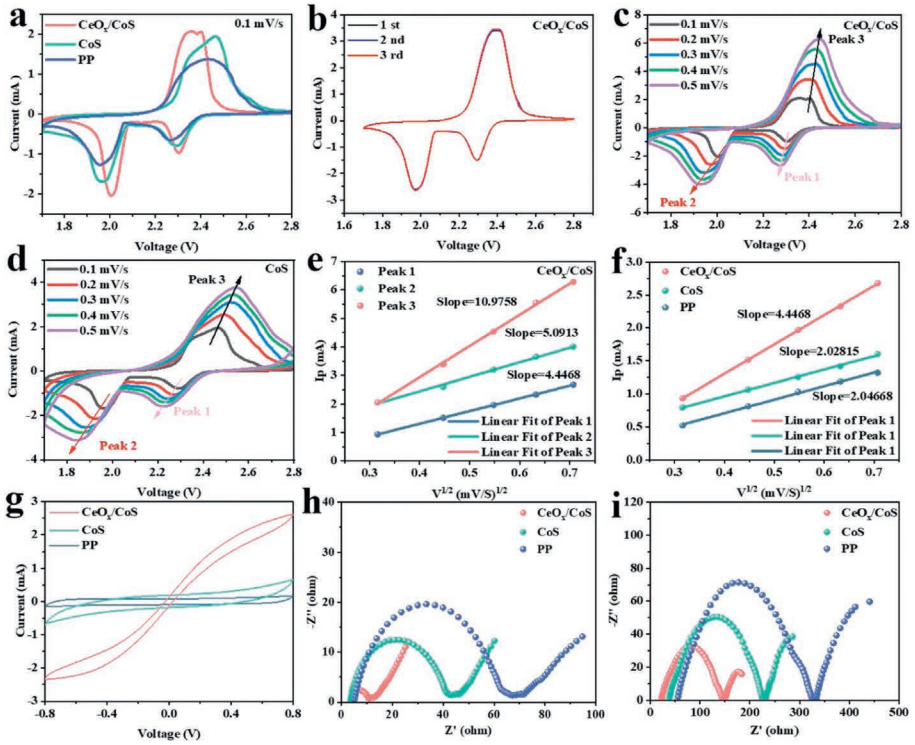



**Fig. 5.** (a) Comparison of CV curves for different separator batteries at a scan rate of 0.1 mV/s. (b) CV curves for the first three cycles at a scan rate of 0.1 mV/s and (c) CV curves at 0.1–0.5 mV/s of $CeO_x$/CoS@PP battery. (d) CV curves at 0.1–0.5 mV/s of CoS@PP battery. (e) Linear fitting curves of redox peaks of $CeO_x$/CoS@PP battery. (f) Comparison of linear fitting curves of reduction peaks of different separator batteries. (g) CV curves of $Li_2S_6$ symmetrical batteries with different separators. (h) EIS curves of different separator batteries. (i) EIS curves of $Li_2S_6$ symmetrical batteries with different separators.

scan rates and the Randles-Sevcik equation can be used to represent their relationship [50–52]:

$$I_p = \left(2.69 \times 10^5\right) n^{3/2} A D_{Li^+}{}^{1/2} C_{Li^+} V^{1/2} \quad (1)$$

where $I_p$ denotes the peak current density, $n$ denotes the number of electrons transferred in the reaction, $A$ denotes the active electrode area, $D_{Li^+}$ denotes the $Li^+$ diffusion coefficient, $C_{Li^+}$ denotes the $Li^+$ concentration, and V denotes the scan rate. According to the equation, it can be seen that a larger slope of the fitted curve indicates a larger $Li^+$ diffusion coefficient (Fig. 5e and Fig. S10 in Supporting information). From the comparison of Fig. 5f and Fig. S11 (Supporting information), it can be directly observed that the slopes of all three peaks of the $CeO_x$/CoS@PP battery are much larger than those of the CoS@PP and PP batteries, which suggests that the synergistic effect between $CeO_x$ and CoS greatly facilitates the $Li^+$ transfer during redox reactions. The higher peak current of the $CeO_x$/CoS@PP battery can be seen from the symmetrical CV curve (Fig. 5g), which also confirms this. We performed EIS measurements to better understand the reason for the improved redox kinetics of the $CeO_x$/CoS@PP separator. As shown in Fig. 5h, the battery using $CeO_x$/CoS@PP separator showed lower impedance than these of CoS@PP and PP batteries, indicating that the conductivity of $CeO_x$/CoS hybrid material is superior to that of pure CoS, and that the presence of this hybrid structure accelerates the rate of charge transfer and ion diffusion. The above CV and EIS measurements indicate that the $CeO_x$/CoS core-shell structure effectively improves the electrochemical reaction kinetics compared to CoS. We further emphasize the strong catalytic role of $CeO_x$/CoS@PP in the kinetics of redox reactions by performing CV and EIS tests on $Li_2S_6$ symmetric batteries. The CV curves of the symmetric batteries at a scan rate of 10 mV/s (delivers the highest peak current among all separator batteries. The EIS curves (Fig. 5i) indicated that the $CeO_x$/CoS@PP battery improved the ionic conductivity and greatly reduced the charge transfer resistance, and these results further demonstrate that the $CeO_x$/CoS heterostructure plays a strong catalytic role in the redox reaction kinetics. The differences in the catalytic performance of $CeO_x$/CoS@PP, CoS@PP and PP diaphragms were further quantified based on the Tafel curve analysis (Fig. S12 in Supporting information). The experimental data showed that the Tafel slope of $CeO_x$/CoS@PP modified diaphragm (88.6 mV/dec) was significantly lower than that of CoS@PP (312 mV/dec) and PP (389 mV/dec), suggesting that the kinetics of its charge-transfer reaction was significantly optimized. The above results further demonstrate that the $CeO_x$/CoS heterostructure significantly reduces the electrochemical polarization and enhances the redox reaction kinetics of LSBs by constructing an efficient bifunctional catalytic interface, which provides a key guarantee for their efficient operation.

Fig. 6a shows the linear scanning voltammetry (LSV) curves of $CeO_x$/CoS@PP, CoS@PP, and PP batteries at a scan rate of 5 mV/s, which illustrated that the $CeO_x$/CoS@PP battery exhibits the best electron transfer rate as well as electrocatalytic reaction kinetics. We further illustrate the effect of different modified materials on the kinetics of the redox reaction by means of nucleation experiments (Figs. 6b and c), the detailed experimental steps of which have been mentioned in the supporting section. The integral areas in the curves indicate the precipitation of $Li_2S$ when $CeO_x$/CoS and CoS materials are used as the cathode of the battery, which are 496.9038 and 234.6795 mAh/g, respectively, it can be clearly observed that $CeO_x$/CoS exhibits the largest peak current as well as the fastest nucleation time. From the equations related to time and peak current, it can be seen that the higher peak current, the faster nucleation time, and the larger nucleation area proved the faster kinetics of the redox reaction [53]. The above experimental results indicate that $CeO_x$/CoS has a strong electrocatalytic ability, which can promote the rapid conversion of LiPSs to $Li_2S$ and accelerate the reaction kinetics. In addition, the internal resistance ($\Delta R$) during charging and discharging was further investigated by

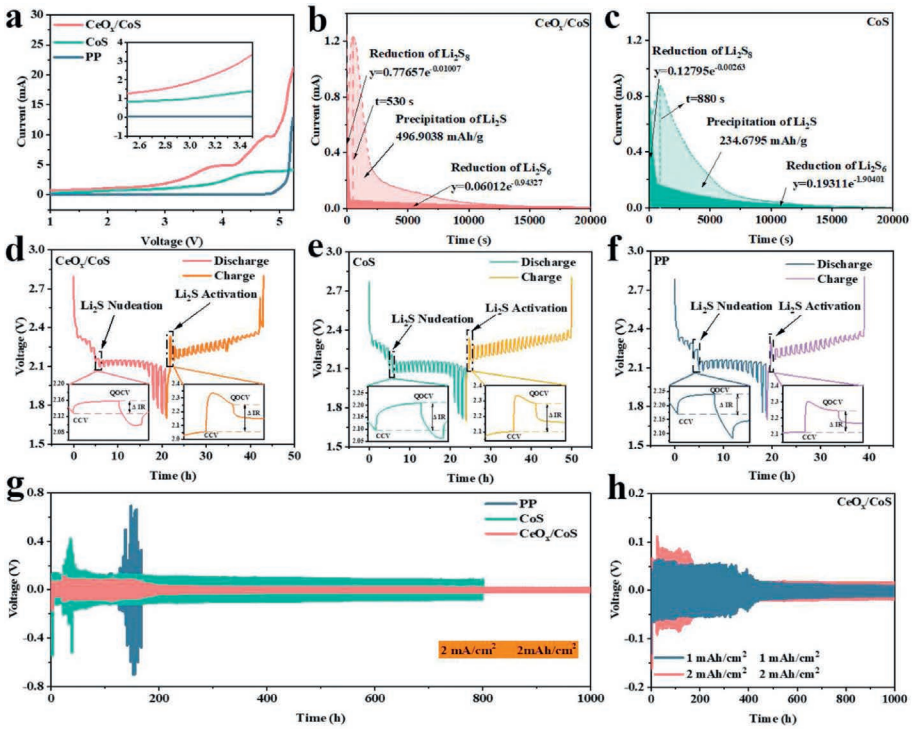



**Fig. 6.** (a) LSV diagram of different batteries. (b, c) Constant potential discharge curves of $Li_2S$ nucleation on $CeO_x$/CoS and CoS electrodes respectively at 2.05 V. (d) GITT curves of $CeO_x$/CoS@PP, (e) CoS@PP and (f) PP batteries. (g) Cycling performance of Li//Li symmetric cells at 2 mA/cm$^2$ for 2 mAh/cm$^2$. (h) Comparison between the cycling performance of Li//Li symmetric batteries at 2 mA/cm$^2$ for 2 mAh/cm$^2$ and at 1 mA/cm$^2$ for 1 mAh/cm$^2$.

measuring the constant-current intermittent titration (GITT) curves of different separator cells at 0.1 C. The $\Delta R$ of $Li_2S$ nucleation and $Li_2S$ activation for the three separator batteries are shown in Figs. 6d-f. $CeO_x$/CoS@PP exhibits the lowest $Li_2S$ nucleation and $Li_2S$ activation internal resistance, which further suggests that it mitigates the hindrance of polarization and reaction kinetics [54]. We explored the modulation effect of $CeO_x$/CoS@PP, CoS@PP, and PP on Li anodes by assembling Li//Li symmetric cells, and measured the long-cycle stability of at a current density of 2 mA/cm$^2$ and an area capacity of 2 mAh/cm$^2$ (Fig. 6g). It can be directly observed that the PP separator cells show a huge voltage hysteresis ($\geq$700 mV) and short circuits after 150 h. On the contrary, the cell with $CeO_x$/CoS@PP exhibits a stable polarization behavior as low as 16 mV and a long cycle life of 1000 h, both exceeding that of CoS@PP and PP, suggesting a significant inhibition of lithium dendrite growth. In addition to this, the long cycle stability of Li//Li symmetric cells were determined at different current densities of 1 and 2 mA/cm$^2$ (Fig. 6h). When the current density is small, the initial overpotential is small and gradually reaches a low and stable polarization behavior (10 mV) after 400 h. When the current density is large, the initial overpotential is large but reaches a low and stable polarization behavior (16 mV) after 180 h. The above results confirm that $CeO_x$/CoS@PP diaphragms can promote uniform $Li^+$ flow and lithium metal plating due to the enhanced modulation effect on $Li^+$ diffusion. The multiplicity performance and lithium deposition/stripping reversibility were tested by cycling Li//Li symmetric cells at variable current densities (0.5–5 mA/cm$^2$, area capacity 2 mAh/cm$^2$). The experimental data show (Fig. S13 in Supporting information) that at a low current density of 0.5 mA/cm$^2$, the polarisation voltage of the $CeO_x$/CoS@PP cell is only 15 mV, which is significantly lower than that of CoS@PP (37 mV) and PP (120 mV). As the current density was increased to 5 mA/cm$^2$, the polarisation voltage was stabilised at 75 mV, while it was as high as 367 mV and 597 mV for CoS@PP and PP, respectively, indicating that the heterostructured diaphragm has excellent current tolerance. All the above parameters confirm that $CeO_x$/CoS@PP diaphragms provide an efficient solution strategy for high-performance LSBs systems by synergistically optimizing the electrocatalytic activity, charge transport ability and interfacial stability. Then, the battery was disassembled after cycling to practically analyze the effect of $CeO_x$/CoS@PP on Li anode. Obviously, it is observed that many bulk particles and cracks on the anode surface for PP and CoS@PP cells (Figs. S14a-d in Supporting information). In contrast, the cell with $CeO_x$/CoS@PP has smooth anode surface (Figs. S14e and f in Supporting information).

The adsorption effect of $CeO_x$/CoS material was further explored by $Li_2S_6$ adsorption test (Fig. 7a), and the yellow solution was lightened after adsorption. From the comparison plots of the XPS survey spectra (Fig. 7b) as well as the fine spectra before and after $CeO_x$/CoS adsorption, it is clearly noticed that the peaks of each element are shifted to higher binding energies in the high-resolution XPS spectra, where the binding energy of Ce 3d shows a shift to the left of about 0.2 eV (Fig. 7c) while that of Co 2p is about 0.3 eV (Fig. 7d). And this result is attributed to the higher electronegativity of $Li_2S_6$, and the transfer of electrons from each component to $Li_2S_6$. The analysis can be further confirmed by the high-resolution XPS spectra of S 2p in Fig. 7e. The intensities of its two significant peaks originally located at 161.5 and 163.2 eV corresponding to S $2p_{3/2}$ and S $2p_{1/2}$ become weaker, and the intensity of the peak located at 168.9 eV corresponding to S $2p_{3/2}$ increases and shifts to a higher binding energy, suggesting that $CeO_x$/CoS reacts significantly with S in $Li_2S_6$ to generate sulfate. The above results further illustrate that $CeO_x$/CoS plays a crucial role in the chemisorption of $Li_2S_6$. As shown in Fig. 7f, we observed the high permeation resistance of the three separators to soluble LiPSs by H-type device permeation experiments. It can be intuitively seen that the $Li_2S_6$ electrolyte on the left side of the PP separator permeates completely to the right side after 12 h, while

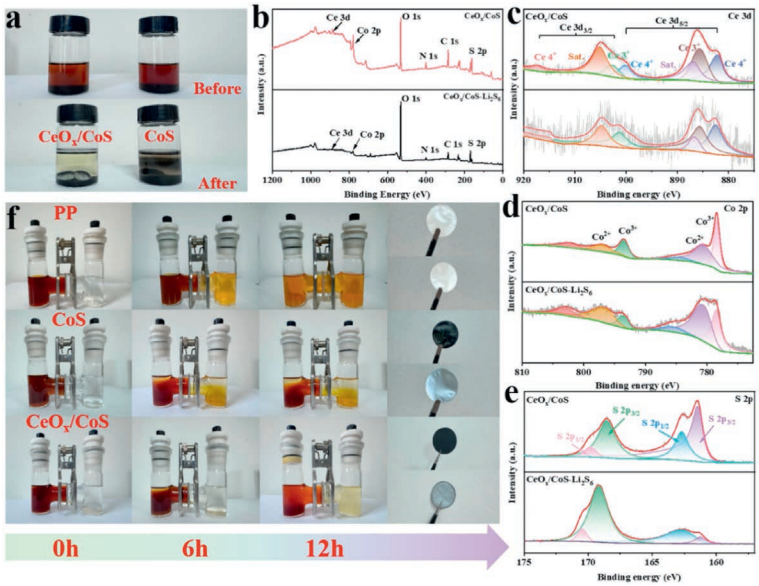



**Fig. 7.** (a) Experiments on the adsorption of $Li_2S_6$ by $CeO_x$/CoS. (b) XPS survey spectrums, (c) Ce 3d, (d) Co 2p and (e) S 2p of adsorbed $CeO_x$/CoS in $Li_2S_6$. (f) Experimental permeation of $Li_2S_6$ to different separators.

the $CeO_x$/CoS@PP separator almost has only slight permeation after 12 h, which shows the strongest blocking performance and greatly inhibits the shuttle effect of LiPSs. To further demonstrate the adsorption and catalytic performance of the $CeO_x$/CoS hybrid material, we disassembled different separator cells that underwent 900 long cycles at 1 C to observe the separator morphology (Figs. S10a-f). Disordered dendritic surfaces appeared on the surface of the PP separator, which affected the transfer of $Li^+$ and electrons (Figs. S15a and b in Supporting information). The surface material of the CoS separator presents a large-area lump-like accumulation with low porosity (Figs. S15c and d in Supporting information). In sharp contrast, the $CeO_x$/CoS separator has a rough and porous surface with high porosity (Figs. S15e and f in Supporting information), which enhances its chemical adsorption capacity for LiPSs. Therefore, the shuttle effect of LiPSs has been alleviated, and the battery cycle performance has been greatly improved.

In summary, double-shelled $CeO_x$/CoS hollow nanobox were successfully prepared through ZIF-67 template and the following growth of $CeO_x$ nanodots from hydrothermal method, which presented high electrical conductivity and electrolyte wettability. When applied as the LSBs PP separator modifier, it can greatly accelerate the conversion reaction kinetics and hinder the shuttle effect of LiPSs. In the $CeO_x$/CoS heterostructures, the abundant porous structure of the CoS surface with enough cavities ensures the fast transport of electrolytes/ions and provides more active catalytic sites. While functional $CeO_x$ nanodots can anchor soluble LiPSs through physical barrier or chemisorption, which can also promote the catalytic conversion of LiPSs and accelerate the sulfur redox kinetics. The results deliver that the $CeO_x$/CoS@PP battery exhibits excellent cycling stability with the capacity remaining at 502.2 mAh/g at 1 C after 900 cycles (decay rate: 0.057 %). When the sulfur loading increased to 4.480 mg/cm$^2$, the capacity retention was maintained 94.5 % after 100 cycles. This study demonstrates the success preparation of novel high catalytic heterostructure and the modification strategy with fast kinetics and efficiently promote LiPSs adsorption/catalytic conversion in LSBs.

## CRediT authorship contribution statement

**Xinyun Liu:** Writing – original draft, Investigation. **Long Yuan:** Data curation. **Xiaoli Peng:** Formal analysis. **Shengjun Lu:** Project administration. **Shilan Li:** Methodology. **Shengdong Jing:** Software. **Hua Lei:** Writing – review & editing, Supervision. **Yufei Zhang:** Writing – review & editing, Supervision. **Haosen Fan:** Writing – review & editing, Supervision.

## Declaration of competing interest

The authors declare that they have no known competing financial interests or personal relationships that could have appeared to influence the work reported in this paper.

## Acknowledgments

This work was supported by National Natural Science Foundation of China (Nos. 52472194, 52101243), Natural Science Foundation of Guangdong Province, China (Nos. 2025A1515012571, 2025A1515010345, 2023A1515012619) and the Science and Technology Planning Project of Guangzhou (No. 202201010565). We would like to thank Analysis and Test Center of Guangzhou University for their technical support (XRD, PW3040/60).

## Supplementary materials

Supplementary material associated with this article can be found, in the online version, at doi:10.1016/j.cclet.2025.111438.

## References

[1] W.G. Lim, S. Kim, C. Jo, J. Lee, Angew. Chem. Int. Ed. 58 (2019) 18746–18757.
[2] Z.Q. Zhou, J. Xiong, Y.F. Zhang, et al., Mater. Today Chem. 52 (2026) 103387.
[3] Q. Zou, Y. Sun, Z. Liang, W. Wang, Y.C. Lu, Adv. Energy Mater. 11 (2021) 2101552.
[4] L. Chen, Z. Liu, W. Yang, et al., J. Colloid Interface Sci. 666 (2024) 416–423.
[5] R. Fang, S. Zhao, Z. Sun, et al., Adv. Mater. 29 (2017) 1606823.
[6] X.C. Guo, M.Y. Chen, Z.J. Yang, et al., Chem. Eng. J. 529 (2026) 172604.
[7] L. Yuan, X.Y. Liu, X.L. Peng, et al., J. Colloid Interface Sci. 698 (2025) 138065.
[8] P. Yang, C.F. Lin, J. Zhou, et al., Chin. Chem. Lett. 37 (2026) 111810.
[9] S. Jing, X.L. Peng, S.L. Li, Chin. Chem. Lett. 36 (2025) 110732.
[10] B. Wang, L. Wang, D. Ding, et al., Adv. Mater. 34 (2022) 2204403.
[11] T. Li, X. Bai, U. Gulzar, et al., Adv. Funct. Mater. 29 (2019) 1901730.
[12] X.Y. Liu, L. Yuan, X.L. Peng, et al., Chin. Chem. Lett. 36 (2025) 110369.
[13] Q. Pang, X. Liang, C.Y. Kwok, L.F. Nazar, Nat. Energy 1 (2016) 1–11.
[14] S.Y. Dong, X.Y. Jin, P. Xia, et al., Mater. Today Chem. 45 (2025) 102654.
[15] W. Bao, L. Liu, C. Wang, et al., Adv. Energy Mater. 8 (2018) 1702485.
[16] D. Wang, Q. Cao, L. Li, et al., ACS Appl. Mater. Interfaces 13 (2021) 16374–16383.

[17] W. Yao, J. Xu, L. Ma, et al., Adv. Mater. 35 (2023) 2212116.
[18] M. Chen, M. Shao, J. Jin, et al., Energy Storage Mater. 47 (2022) 629–648.
[19] H. Wang, Y. Wei, G. Wang, et al., Adv. Sci. 9 (2022) 2201823.
[20] Z. Wang, Y. Li, H. Ji, et al., Adv. Mater. 34 (2022) 2203699.
[21] Y. Li, X. Zhang, Q. Zhang, et al., ACS Appl. Mater. Interfaces 14 (2022) 18634–18645.
[22] Y. Yan, P. Zhang, Z. Qu, et al., Nano Lett. 20 (2020) 7662–7669.
[23] B. Wang, L. Wang, B. Zhang, et al., ACS Nano 16 (2022) 4947–4960.
[24] T. Liu, H. Li, J. Yue, et al., Angew. Chem. Int. Ed. 60 (2021) 17547–17555.
[25] W.J. Chen, B.Q. Li, C.X. Zhao, et al., Angew. Chem. Int. Ed. 59 (2020) 10732–10745.
[26] X.Y. Jin, X.C. Guo, S.Y. Dong, et al., Chin. Chem. Lett. 36 (2025) 110604.
[27] W. Yao, C. Tian, C. Yang, et al., Adv. Mater. 34 (2022) 2106370.
[28] P.F. Wan, X.C. Guo, S.D. Jing, et al., Chem. Eng. J. 504 (2025) 159014.
[29] J. Song, C. Zhang, X. Guo, et al., J. Mater. Chem. A 6 (2018) 16610–16616.
[30] Y. Liu, X. Qin, S. Zhang, et al., ACS Appl. Mater. Interfaces 10 (2018) 26264–26273.
[31] B. Qi, X. Zhao, S. Wang, et al., J. Mater. Chem. A 6 (2018) 14359–14366.
[32] Z.A. Ghazi, X. He, A.M. Khattak, et al., Adv. Mater. 29 (2017) 1606817.
[33] W. Weng, V.G. Pol, K. Amine, Adv. Mater. 25 (2013) 1608–1615.
[34] H. Li, M. Sun, T. Zhang, Y. Fang, G. Wang, J. Mater. Chem. A 2 (2014) 18345–18352.
[35] T. Wang, K. Kretschmer, S. Choi, et al., Small Methods 1 (2017) 1700089.
[36] X. Jiang, X. Zhu, X. Ai, H. Yang, Y. Cao, ACS Appl. Mater. Interfaces 9 (2017) 25970–25975.
[37] S.H. Chung, A. Manthiram, Adv. Funct. Mater. 24 (2014) 5299–5306.
[38] W. Yao, J. Xu, Y. Cao, et al., ACS Nano 16 (2022) 10783–10797.
[39] M. Wang, Y. Zhu, Y. Sun, et al., Adv. Funct. Mater. 33 (2023) 2211978.
[40] J.L. Yang, D.Q. Cai, Q. Lin, et al., Nano Energy 91 (2022) 106669.
[41] J. Lopez, D.G. Mackanic, Y. Cui, Nat. Rev. Mater. 4 (2019) 312–330.
[42] L. Chen, Z. Liu, W. Yang, et al., J. Colloid Interface Sci. 666 (2024) 416–423.
[43] K. Chen, G. Zhang, L. Xiao, et al., Small Methods 5 (2021) 2001056.
[44] S.B. Wu, X.T. Li, Y.F. Zhang, et al., Chem. Eng. Sci. 313 (2025) 121737.
[45] J. Chu, Y. Wang, F. Zhong, et al., EcoMat 3 (2021) e12133.
[46] S.L. Li, S.D. Jing, X.L. Peng, et al., Mater. Today Chem. 43 (2025) 102488.
[47] T. Montini, M. Melchionna, M. Monai, P. Fornasiero, Chem. Rev. 116 (2016) 5987–6041.
[48] C.I. Hiley, H.Y. Playford, J.M. Fisher, et al., J. Am. Chem. Soc. 140 (2018) 1588–1591.
[49] H. Xu, J. Cao, C. Shan, et al., Angew. Chem. Int. Ed. 130 (2018) 8790–8794.
[50] S.M. Wu, Y.N. Li, L.T. Chen, et al., Chin. Chem. Lett. 36 (2025) 109796.
[51] F. Xu, S.L. Li, S.D. Jing, et al., J. Colloid Interface Sci. 660 (2024) 907–915.
[52] S.L. Li, S.D. Jing, X.L. Peng, et al., Chin. Chem. Lett. 37 (2026) 111731.
[53] S. Fu, H. Wang, Y. Zhong, et al., Adv. Mater. 35 (2023) 2302771.
[54] Z. Wu, S. Chen, L. Wang, et al., Energy Storage Mater. 38 (2021) 381–388.